



Article

Monitoring Spatial–Temporal Variations in River Width in the Aral Sea Basin with Sentinel-2 Imagery

Jingjing Zhou ¹, Linghong Ke ^{1,*} , Xin Ding ¹, Ruizhe Wang ¹ and Fanxuan Zeng ²¹ College of Geography and Remote Sensing, Hohai University, Nanjing 210098, China² Key Laboratory of Watershed Geographic Sciences, Nanjing Institute of Geography and Limnology, Chinese Academy of Sciences, Nanjing 210008, China

* Correspondence: kelinghong@hhu.edu.cn

Abstract: Rivers in arid regions serve as crucial freshwater resources for local communities and play an essential role in global hydrological and biogeochemical cycles. The Aral Sea Basin (ASB) in Central Asia is characterized by an arid climate and river dynamics that are sensitive to climate change and human activities. Monitoring the spatiotemporal variations in river water extent in the ASB is essential to maintain an ecological balance and ensure water security. In this study, we extracted data regarding monthly river water bodies in the ASB from 2017 to 2022 by synthesizing monthly Sentinel-2 images. The water extents on the Sentinel images were automatically mapped using the Otsu method, and the river widths for all river channels were calculated using the RivWidth algorithm. We investigated the relationships between the river dynamics and the geomorphology, climatic change, human activities, and the annual and interannual variations in the river width in different reaches of the basin. The results show a seasonal variability in the river width, with most rivers reaching the largest width in the warm season and a few rivers in the middle and lower areas reaching the valley value in the warm season. Compared to their tributaries, the mainstem in the middle/lower regions showed less seasonal variability. According to interannual analysis, most of the rivers in the ASB significantly narrowed between 2017 and 2022, a phenomenon which is generally impacted by temperature and evapotranspiration variations. Comparisons show that our results provide improved information about the narrow river reaches and denser river networks compared to the previous global dataset, demonstrating the advantageous properties of high spatial resolution in Sentinel-2 imagery.

Keywords: river dynamics; seasonal variability; interannual variation; Google Earth Engine; climatic variations



Citation: Zhou, J.; Ke, L.; Ding, X.; Wang, R.; Zeng, F. Monitoring Spatial–Temporal Variations in River Width in the Aral Sea Basin with Sentinel-2 Imagery. *Remote Sens.* **2024**, *16*, 822. <https://doi.org/10.3390/rs16050822>

Academic Editor: Won-Ho Nam

Received: 13 January 2024

Revised: 9 February 2024

Accepted: 24 February 2024

Published: 27 February 2024



Copyright: © 2024 by the authors. Licensee MDPI, Basel, Switzerland. This article is an open access article distributed under the terms and conditions of the Creative Commons Attribution (CC BY) license (<https://creativecommons.org/licenses/by/4.0/>).

1. Introduction

River systems are essential components of the global hydrological cycle and are crucial to the health of the worldwide ecosystem and climate system [1,2]. Rivers play a crucial role in supplying essential freshwater resources for human communities and ecosystems, serving as indispensable lifelines for regional economic development, environmental sustainability, and ecological security [3–5]. At the same time, rivers play a significant role as sources of greenhouse gas emissions, contributing substantially to the outgassing of carbon dioxide and methane into the atmosphere [6]. It is essential to monitor the spatiotemporal dynamics of rivers for applications in hydrology [7–10], climate change research [11–13], fluvial geomorphology [14,15], stream ecology [4], water management [16], and flood prediction [17].

The traditional methods of monitoring river dynamics depend on in situ observations from field studies and gauging stations, which have a limited spatial and temporal resolution coverage because of logistical difficulties and political and economic circumstances [18,19]. The rapid development of remote sensing has advanced the way of monitoring surface water dynamics at a spatial scale previously impossible [20], with the

advantages of a global coverage, low cost, and periodical operations [21–23]. Surface water dynamics have been extensively observed using various remote sensing data. Recent studies have mainly focused on extracting surface water extents using Landsat imagery [24,25], which, since 1984, has captured multispectral images of the Earth with a spatial resolution of 30 m [26]. With the development of open acquisition platforms such as the Google Earth Engine (GEE) platform [27], many researchers have successfully used Landsat images to produce regional or global river geomorphology datasets (Table 1). Yamazaki (2014) [28] created the Global Width Database for Large Rivers (GWD-LR) by combining hydrologic data with the maps derived from multiscale Shuttle elevation derivatives and Landsat images for large rivers (width > 300 m). Allen and Pavelsky (2015) [29] developed the NARWidth dataset, which calculated river widths in North America at mean discharge times using the RivWidth tool. Allen and Pavelsky (2018) [11] produced a more fine-grained product, Global River Widths from Landsat (GRWL), for rivers greater than 30 m under average annual flow conditions on a global scale. The Multitemporal China River Width (MCRW) dataset, developed by Yang (2020) [30], stands as China’s inaugural 30 m multi-temporal river width dataset spanning from 1990 to 2015. This dataset encompasses seasonal variations and provides estimates for dynamic inundation frequencies.

Table 1. The current river width datasets derived from satellite imagery.

Name and Abbreviation	Spatial Coverage	Baseline Data	Temporal Coverage	Nominal Resolution	Data Source
GWD-LR	Global	SRTM	11 February 2000–22 February 2000	90 m	Yamazaki et al., 2014 [28]
NARWidth	North America	Landsat	N/A	30 m	Allen and Pavelsky, 2015 [29]
GRWL	Global	Landsat	N/A	30 m	Allen and Pavelsky, 2018 [11]
MCRW	China	Landsat	1990–2015	30 m	Yang, J. et al., 2020 [30]

However, due to spatial resolution limitations, Landsat imagery has restricted coverage for rivers narrower than 30 m in width, making it challenging to identify the morphological and topological characteristics of the small rivers or seasonal streams that are standard in arid or semi-arid regions. Furthermore, current river extent datasets mainly reflect a static status of rivers under specific meteorological or hydrological conditions, which cannot provide information on the temporal variabilities of rivers. The spatiotemporal details are urgently needed to enhance river observations, especially for small rivers (width < 30 m) and seasonal rivers that are widely distributed in arid, semi-arid, or high-altitude regions. High-resolution satellite imagery, such as Sentinel-2 images, provides a solution for detailed river channel extraction, with a finer spatial resolution of 10 m and a higher revisit frequency (approximately five days) [31] compared to the Landsat imagery. With these advantages, Sentinel-2 images show potential for the improved monitoring of small surface water bodies and water dynamics on land surfaces [32–34].

Since the 1960s, water resources in Central Asia have undergone noticeable changes attributed to climate change, increasing water demands, and human interventions [35,36]. The substantial reduction of the Aral Sea has transformed it into a primary source of dust storms carrying diverse pollutants, leading to a significant ecological crisis. A recent study indicates that approximately 54.37% of Central Asia’s surface water faces the threat of recession and desiccation [37]. In addition, the demand for water in agriculture and large-scale irrigation systems typically relies on the ASB, where the population has tripled from 1960 to 2015 [38]. Therefore, monitoring the river dynamics in the ASB is essential for effective water administration and management to ensure the sustainability of freshwater resources.

The investigation into the river dynamics of the ASB has been constrained, primarily due to the challenges associated with obtaining and processing time-series images across extensive regions [39,40]. Rivers in the ASB are typically small rivers or seasonal streams originating from the uninhabited high-mountain areas, which are challenging to capture with coarse-resolution imagery. The overall basin-scale river dynamics of the ASB and their variations among sub-basins remain unknown. This study, focusing on the ASB, addresses this gap and aims to explore the potential of Sentinel-2 images for monitoring river dynamics in a typically dry region. The primary objectives include developing an automated

method for retrieving the time series of water extents and parameters of rivers based on Sentinel-2 imagery as well as investigating the spatiotemporal variations in river width in the ASB during 2017–2022. We present an automated method for extracting the water extent and river width over extensive regions from Sentinel imagery by taking advantage of the GEE computational resource and synthesis of algorithms for river network extraction. We analyzed river dynamics, including seasonal and interannual variations across different regions, to better understand the spatiotemporal variations in this region and their relationships with the climate, topography, and anthropogenic factors. The insights gained from this study will be valuable for the decision makers involved in informed water resource management, understanding and predicting the impacts of climate change, and implementing strategies for ecological balance and water security in the ASB.

2. Study Area

The Aral Sea Basin (ASB) is an endorheic basin lying in the abdomen of Eurasia and the west of the Tibetan Plateau, with an area of about $1.64 \times 10^4 \text{ km}^2$ (Figure 1). The Amu Darya and Syr Darya, the two main rivers of the basin, flow into the Big and Small Aral Seas, respectively. The Amu Darya is the largest river in Central Asia, with a total length of approximately 2400 km, originating from the glaciers and snowfields of the western Tien Shan Mountains and Pamir Mountains of Tajikistan [41,42]. The Syr Darya, the longest river in Central Asia, flows from the Tien Shan mountains and displays mostly nivo-glacial feeding, with a length of 3019 km to the Aral Sea [43,44]. The rivers and lakes in the arid inland region receive significant water from the glaciers and seasonal snow covering the eastern and southeastern mountainous regions. The region hosts 2737 glaciers covering an area of 1283 km² [45], serving as a crucial water source and a long-term reservoir for freshwater. The middle–west regions are plain desert areas and Aral Sea lakes, which receive river recharge from precipitation and snow meltwater. We further divide the ASB into seven subregions for this study to evaluate the river width variations, as shown in Figure 1.

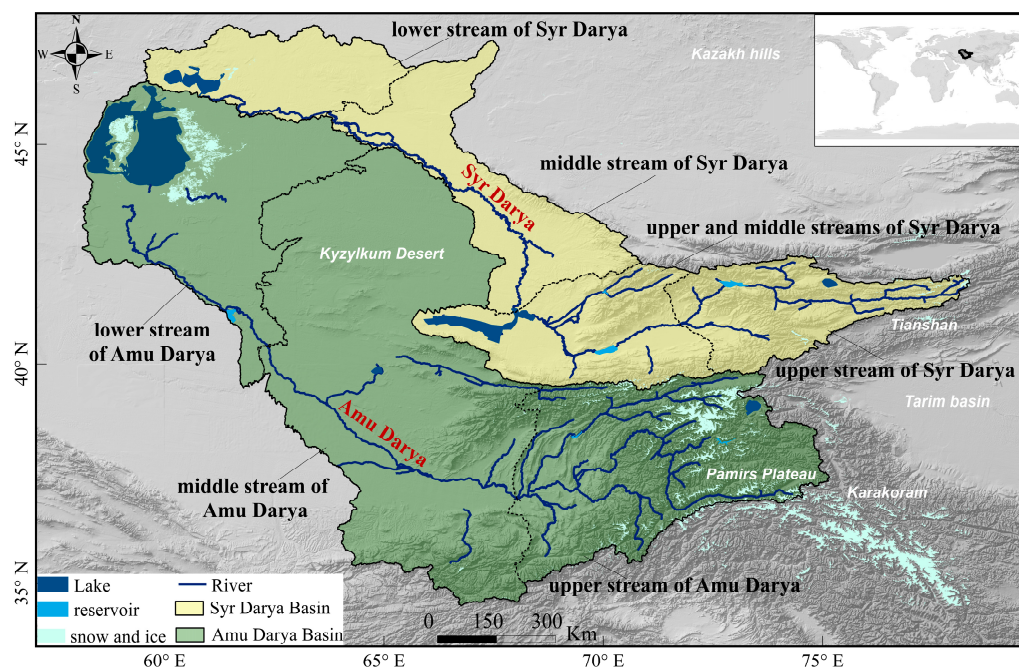


Figure 1. An overview of the Aral Sea Basin. Rivers, lakes, and reservoirs are from the JRC GSW dataset and the HydroLAKES database. Glaciers are from the GAMDAM glacier inventory. The seven subregions include the upper stream of the Amu Darya (upper AMU), the upper stream of the Syr Darya (upper SYR), the middle stream of the Amu Darya (middle AMU), the middle stream of the Syr Darya (middle SYR), the upper and middle streams of the Syr Darya (upper/middle SYR), the lower stream of the Amu Darya (lower AMU), and the lower stream of the Syr Darya (lower SYR).

With mountains in the southeast blocking the warm, humid air currents from the Indian and Pacific Oceans entering into the basin [46], the ASB is under a typical continental arid and semi-arid climate characterized by a cold winter and hot summer, an uneven distribution of precipitation, and generally high diurnal and seasonal variations in temperature [47]. In January, the average temperatures range from 0 °C to 4 °C, while in July, they range from 28 °C to 32 °C, with even higher temperatures in the desert regions [48]. The primary source of humidity is the westerlies from the Atlantic, and the precipitation patterns are mainly influenced by the interplay between the Siberian anticyclone in the winter (resulting in dry conditions) and cyclonic activity from the west in the summer (leading to wet conditions) [49]. Water vapor fluxes mainly come from the North Atlantic and Indian Oceans and are transported by the westerly wind belt and the South Asian monsoon [50–52]. Precipitation in Central Asia is concentrated in the spring and early summer, especially in the spring. The warm-season average precipitation from 1960 to 2015 was 17.3 mm, while the cold-season average was 22.9 mm [53]. The precipitation is highest in mountainous areas and lowest in the central and western parts of the basin [54].

3. Data and Methods

3.1. Data

3.1.1. Sentinel-2 MSI Imagery

The European Space Agency (ESA) initiated the Copernicus program, in which two new Earth observation satellites for the Sentinel-2 mission have been developed (<https://sentinel.esa.int/web/sentinel/missions/sentinel-2>, accessed on 19 December 2021). The two identical satellites, Sentinel-2A and Sentinel-2B, were launched on 23 June 2015 and 7 March 2017. The satellites carry a multispectral imaging (MSI) sensor to acquire images with a high return frequency (10 days for one satellite, five days for two satellites), which is advantageous for dynamic surface water mapping and monitoring [32]. Sentinel-2 provides two main products: Level-1C and Level-2A. Level-1C represents the top of atmosphere (TOA) reflectance after affine variation and geometric correction, while Level-2A signifies the surface reflectance after atmospheric correction. We used the Sentinel-2 Level-1C product on the GEE platform for surface water mapping, as TOA reflectance is sufficient for the identification of surface water, and atmospheric corrections may introduce additional uncertainties [55].

Sentinel-2 MSI captures 13 spectral bands ranging from visible light and near-infrared (VNIR) to shortwave infrared (SWIR) [31]. We utilized three bands: GREEN, NIR, and SWIR. The SWIR band, initially at a spatial resolution of 20 m, was resampled to 10 m to match the spatial resolution of the GREEN and NIR bands. We utilized Sentinel-2 satellite images acquired from January 2017 to December 2022. We referenced the “QA60” band to identify and mask cloud pixels on the Sentinel-2 imagery. For quality control, we filtered images with a cloud cover larger than 20%. This threshold was chosen to balance between image quality and quantity. After filtering, we processed a total of 68,144 Sentinel-2 images for the study area. These images were organized into collections based on the calendar month to construct a monthly time series. On average, there are 946 images for each month of the year.

3.1.2. Auxiliary Data

The auxiliary data used in the study included the JRC GSW dataset, HydroBASINS, Height Above the Nearest Drainage (HAND) dataset, and the ERA5-Land monthly dataset, which globally will be acquired and integrated into the Google Earth Engine (GEE) platform. The Joint Global Surface Water Research Center (JRC GSW) dataset is a comprehensive and widely used dataset developed by the European Commission. It reveals the substantial spatiotemporal changes in the global surface water over the past 37 years. This dataset provided detailed information on the changes in surface water extents and offered valuable insight into changes such as the expansion or contraction of water bodies, seasonal fluctuations, and long-term trends. The JRC product comprises seven bands, and this study utilizes the

maximum water extent (GSW MWE) in the dataset to mitigate the impact of background noise, representing all locations where water has been detected from 1984 to 2018.

The HydroBASINS dataset provides boundaries of global basins organized in 12 scales according to the Pfafstetter coding system [56]. The HydroBASINS database's continuous global coverage of level-6 basins served as the fundamental scale for segmenting river reaches in the study area. Due to the potential misclassification of terrain shadows as water bodies, we used SRTM DEM data to mask the regions in mountainous areas with slopes exceeding 15 degrees. The Shuttle Radar Topography Mission (SRTM) Digital Elevation Model (DEM) is a high-resolution global digital elevation model that has been widely used for topographic mapping and hydrological modeling [57]. Additionally, we used the HAND (Height Above the Nearest Drainage) dataset [58] to mask topographic shadow regions in flat areas with a threshold of 30. The ERA5-Land monthly dataset [59] is a reanalysis dataset that provides comprehensive monthly climate information at $0.1^\circ \times 0.1^\circ$. Compared to ERA5, this dataset provides an enhanced view of the changes in land features over the decades. It is a valuable resource for investigating the relationships between river dynamics and various climate factors.

3.2. Methods

The flowchart of methods consists of three main steps to derive and analyze the time series of river maps (Figure 2). First, we pre-processed the Sentinel-2 images to mask cloud pixels and eliminate possible terrain shadows on the GEE platform. Secondly, two water indices were employed as input for Otsu's threshold segmentation method to automate the extraction of water bodies. Then, the RivWidth algorithm [60] was used to extract the river centerline and calculate the river width based on the water mask. Finally, we explored the spatiotemporal patterns of river dynamics, conducted a qualitative verification, and analyzed the driving mechanism. The details are organized in the sections as follows:

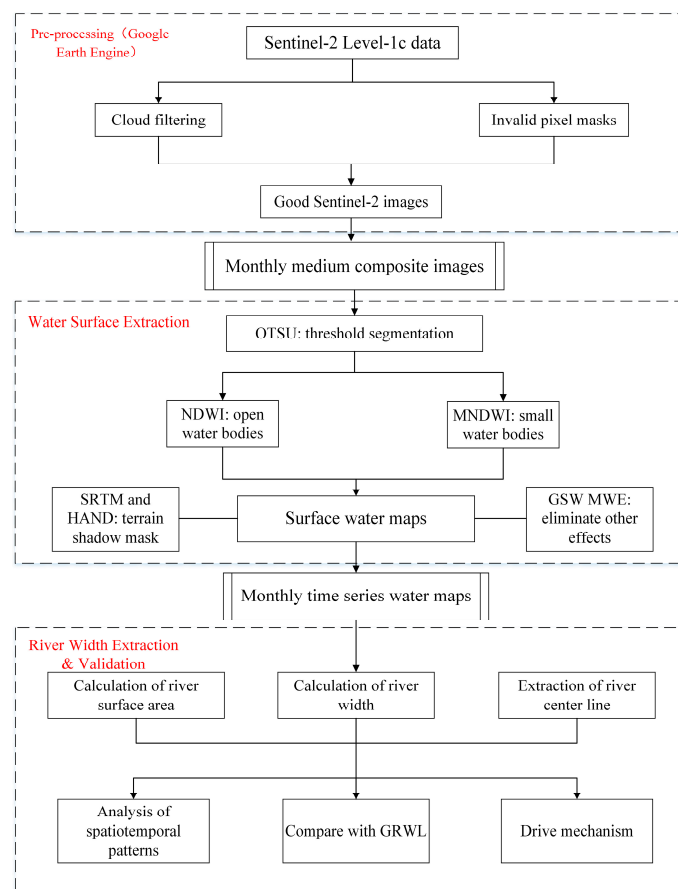


Figure 2. The technical flowchart for the river extraction and river width calculation.

3.2.1. Water Extraction

To maximize the differentiation between water and non-water on Sentinel images, we used the NDWI proposed by McFeeters (1996) [61] and the MNDWI water index developed by Xu (2006) [62] as basic references. The NDWI formula (Equation (1)) is expressed as follows:

$$\text{NDWI} = \frac{\rho_{\text{Green}} - \rho_{\text{NIR}}}{\rho_{\text{Green}} + \rho_{\text{NIR}}} \quad (1)$$

where ρ_{Green} and ρ_{NIR} are Band 3 and Band 8, respectively.

The MNDWI formula (Equation (2)) is proposed as follows:

$$\text{MNDWI} = \frac{\rho_{\text{Green}} - \rho_{\text{SWIR}}}{\rho_{\text{Green}} + \rho_{\text{SWIR}}} \quad (2)$$

where ρ_{Green} and ρ_{SWIR} are Band 3 and Band 11, respectively.

The NDWI has been well established and validated in numerous previous studies for mapping water bodies [62–64]. However, its accuracy is relatively low in areas where water, buildings, soil, and vegetation are mixed. By using the MNDWI, this accuracy is significantly improved [32,65,66]. Therefore, it is necessary to compare surface water maps of NDWI and MNDWI products to understand the influence of built-up and mixed pixels, especially in riverbanks and construction zones. We compared two surface water maps by visually evaluating the water boundaries on several cloud-free subsets. We selected the optimal surface water detection maps for our study area based on visual interpretations.

The Otsu algorithm has been confirmed to be an effective tool for determining the threshold of the water index for surface water mapping [67–69]. The Otsu algorithm finds an optimal threshold that maximizes the variance between the target and the background class, which can be done through a histogram analysis of the pixel values (e.g., NDWI) [70]. Once the threshold is determined, the image is segmented into water (above the threshold) and background (below the threshold). Using the automatic Otsu tool developed by Nobuyuki [71], we dynamically determined the threshold for different river reaches and retrieved water pixels based on the NDWI and MNDWI maps. The improvement we made was to use the GSW maximum water extent to create buffer mask data to define the extent of the histogram statistics. With a narrowed spatial extent, the accuracy of Otsu's classification of water bodies can be improved with a precise bimodal distribution.

3.2.2. Data Post-Processing

Background noise, which includes complex topography, vegetation, clouds, snow, and hill shadows, significantly impacts the water extraction accuracy. To reduce the effects of mountain shadows, we employed hydrologically relevant terrain models from the SRTM V3 product. In addition, we utilized the GSW maximum water extent band to reduce the undesirable noise impact and enhance the river extraction efficiency to create distinct buffer zones for various stream-order reaches.

3.2.3. Calculation of River Width and River Surface Area

The influence of clouds, shadows, and bridges resulted in gaps in the water mapping data. Manual topological processing in ArcGIS 10.5 addressed this issue and connected these gaps to ensure a more complete representation of the river network. We used the RivWidth algorithm to extract the river centerline and automatically calculated the river width based on the connected river surface from the water maps. Delineating the outlines of rivers from the binary water maps involves various processing steps (Figure 3).

The RivWidth algorithm generated two final outputs: a width image displaying the entire flow width at each centerline pixel and a spreadsheet containing each pixel's location coordinates and the river's flow width. We converted the binary water map's grid into a vector plane format. After calculating the vector area, we eliminated polygons smaller than 0.01 square kilometers, because they might not actually represent water, but instead, background noise.

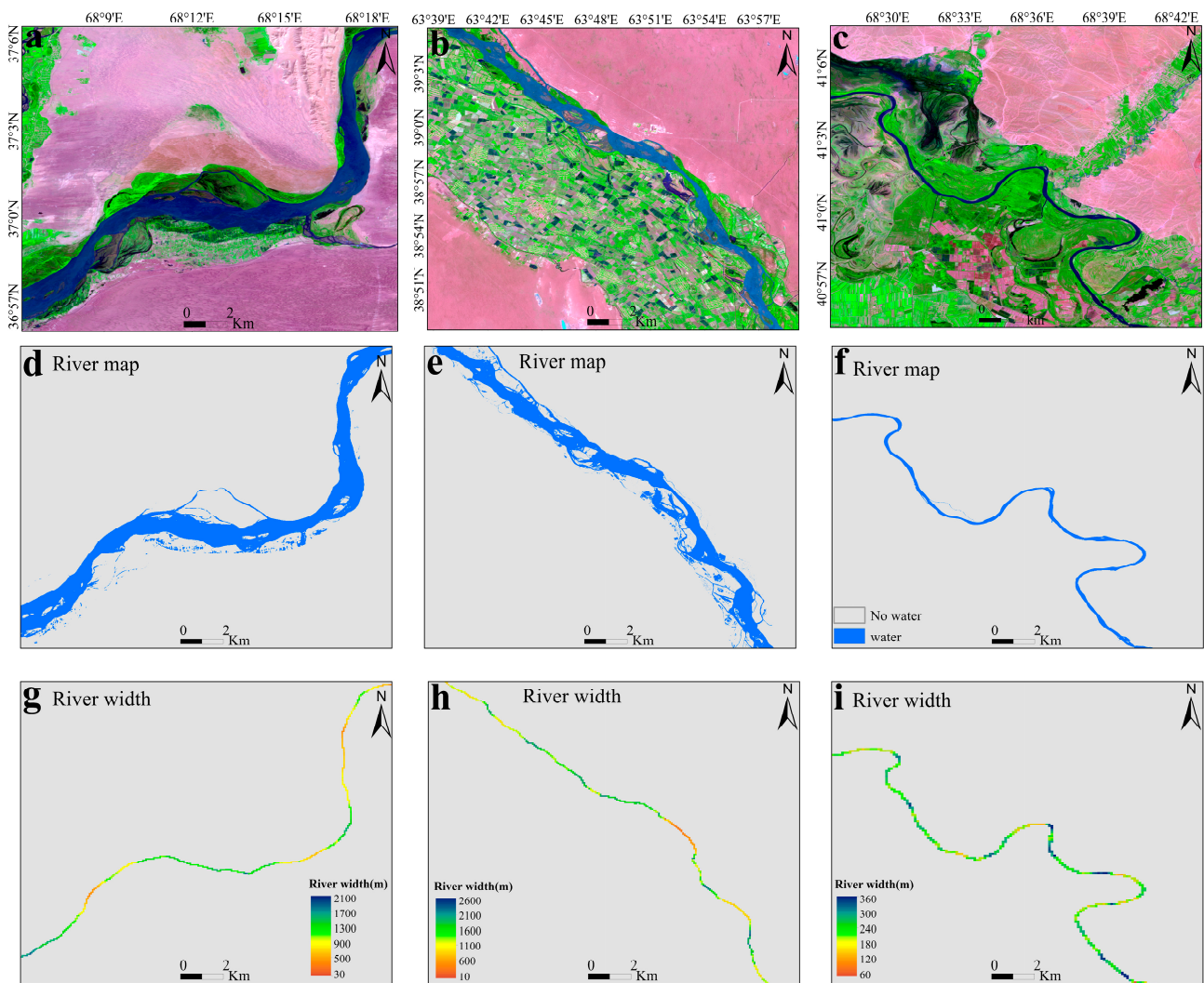


Figure 3. Inputs, intermediate steps, and outputs of river width calculations in this study: (a) simulated true-color composite of Sentinel-2 over the upper reaches of the Amu Darya (37.1°N, 68.6°E); (b) simulated true-color composite of Sentinel-2 over the middle reaches of the Amu Darya; (c) simulated true-color composite of Sentinel-2 for the middle stream of the Syr Darya (41.5°N, 68.8°E); (d–f) are water maps of composited monthly median values for July 2018 corresponding to (a), (b), and (c), respectively; (g–i) are river width maps corresponding to (d), (e), (f), respectively.

3.2.4. Quantifying River Width Variations

This study used monthly composite images from January 2017 to December 2022 to depict river dynamics in the ASB. We chose the level-6 seamless basins from the HydroBASINS database as the fundamental scale for delineating river segments. Each level-6 basin polygon cropped the river centerline to form a separate watershed-scale river network. This results in 170 level-6 basin units covering the study area. We derived a monthly time series of the mean river width for each sub-basin for 2017 and 2022. The time series was aggregated into two seasons: the warm season (April to September) and the cold season (October to March) to depict the seasonal width variability. Considering the width fluctuations in different reaches, the percent variation represents the seasonal width variability. The formula (Equation (3)) is proposed as follows:

$$\frac{(\text{Width}_{\text{warm}} - \text{Width}_{\text{cold}})}{(\text{Width}_{\text{warm}} + \text{Width}_{\text{cold}})} \quad (3)$$

where $\text{Width}_{\text{warm}}$ and $\text{Width}_{\text{cold}}$ denote the mean river width in the warm season and cold season, respectively. For the interannual analysis, we aggregated the monthly time series

of the river width to yearly data. We performed the least-squares regression method to quantify the trends in river width over the years. We evaluated the slope of the regression line to understand the direction and magnitude of the trend. We analyzed the trends and interannual variations in the river width for each basin. We calculated the average river width for the corresponding months during the study period to examine the annual variations in river width.

3.2.5. Qualitative Evaluation

To evaluate the accuracy of the river extraction results from the Sentinel-2 images, we conducted an overlay analysis and qualitative evaluation using the GRWL database [49]. The global river width (>30 m) data are provided by the GRWL database, which uses Landsat imagery. We used various indicators to compare the results in this study with the GRWL database, which include the river network density (ratio of river length to basin area), open-water fraction (ratio of water surface area to basin area), and river connectivity (river length of a single connected reach).

3.2.6. Correlation Analysis

We integrated meteorological data to explore the correlations between climatic variations and river dynamics. The Pearson correlation coefficient is a frequently employed method for assessing the correlation between two variables [72,73]. This study examined the relationship between climatic factors (temperature, precipitation, and evapotranspiration) and river width at different time scales (seasonally, annually, and interannually) to determine the relative contributions of various climatic variables to the river width dynamics. For each subregion and the whole region, we calculated the mean monthly climatic variables from the ERA5-Land monthly dataset and matched them with the corresponding river-width time series for the correlation analysis.

4. Results

4.1. Spatial and Temporal Dynamics of Rivers in the Aral Sea Basin

4.1.1. Distribution of Rivers

Figure 4 depicts the spatial distribution of the river widths in the ASB extracted from median composite Sentinel-2 images. In this investigation, we computed the widths of all rivers, totaling 9.6×10^4 km of rivers in the ASB. The detailed results include the latitude and longitude of pixels on the river centerline and their corresponding widths. Additionally, they form a braiding index field indicating the number of channels in each river section. From the spatial distribution of the river widths shown in Figure 4, we can see that the rivers are narrower in the downstream delta area (Figure 4b) and the upstream headwaters region (Figure 4d). At the same time, the channels widen where tributaries converge (Figure 4c). The minimum width of the rivers is 10 m (corresponding to the minimum pixel size of Sentinel-2 images), and the maximum width can reach up to 4724 m at the intersection of tributaries.

Rivers in the ASB are predominantly concentrated in the eastern part, with most rivers originating from the east region. Rivers are particularly dense in the high-altitude southeastern part, where the sources are fed by glacial and snowmelt water. The river network density in the southeast is higher than in the middle and lower streams in the northwest, reaching a maximum density of 9.0 m^{-1} . The mainstem and tributaries are interleaved in the basin. In the flat plains and desert areas, the density of the river branches decreases and eventually disappears due to agricultural irrigation and human activities. Consequently, the river network density in these areas decreases.

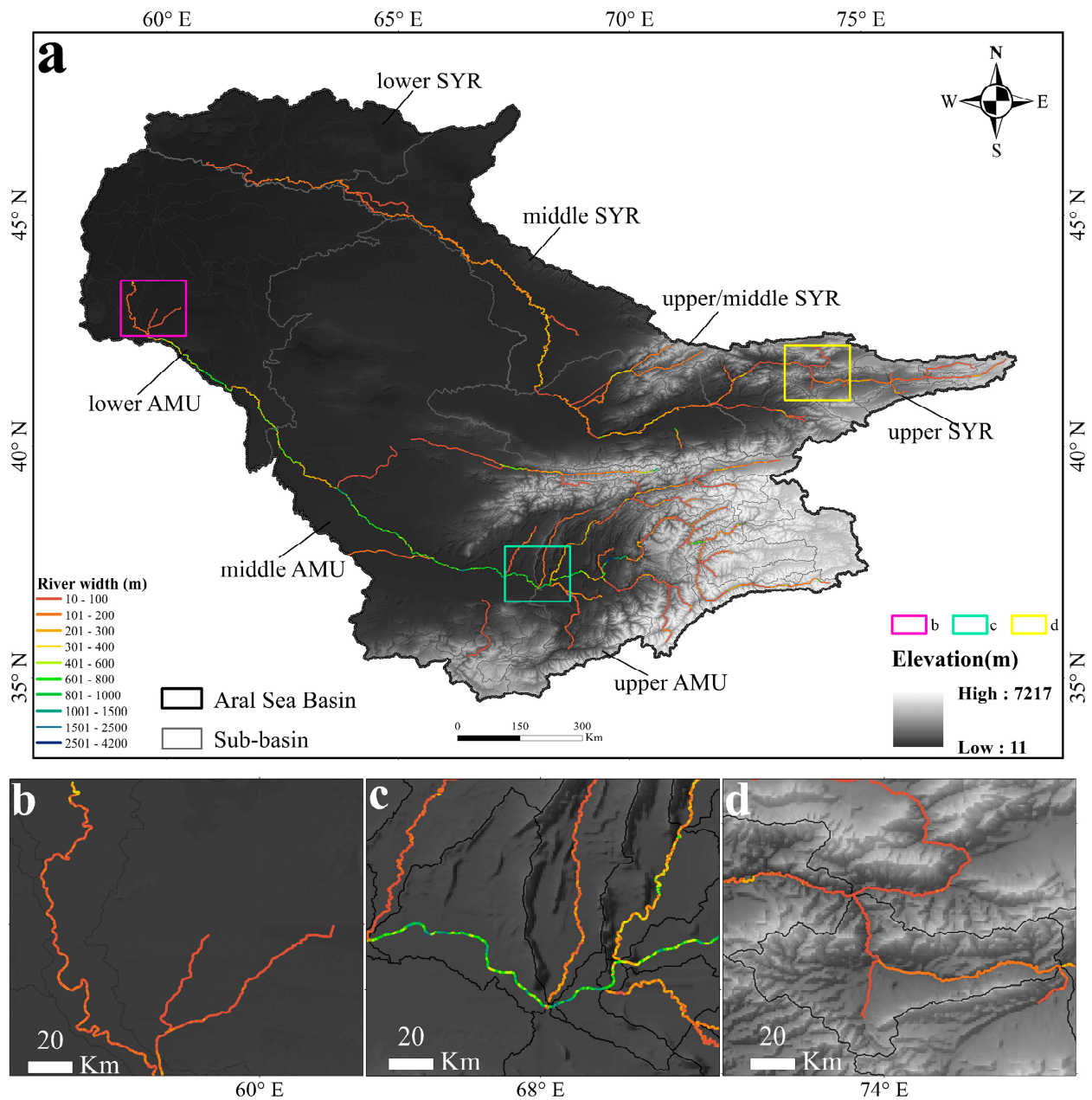


Figure 4. (a) Spatial distribution of river extraction results in the ASB; (b) zoomed-in map of lower stream of the Amu Darya (59.43°E, 42.56°N); (c) zoomed-in map of upper and middle streams of the Amu Darya (68.7°E, 37.28°N); (d) zoomed-in map of upper stream of the Syr Darya (73.41°E, 41.32°N).

4.1.2. Seasonal Variations in River Width

Given the varying climate conditions, the river width in the ASB exhibits different seasonal patterns. We calculated the percentage variation in the river width in the warm and cold seasons to estimate the seasonal variations. Positive values indicate that the river is wider in the warm season, while negative values indicate that the river is wider in the cold season. According to the results, the river is wider in the warm season for the majority of the river reaches the Amu Dara and the middle and upper streams of the Syr Darya (Figure 5a). Meanwhile, we observe the largest river width in the cold season in specific river reaches (e.g., the lower and a proportion of the middle streams of the Syr Darya). This phenomenon may be related to the climatology, mostly seasonal precipitation distribution.

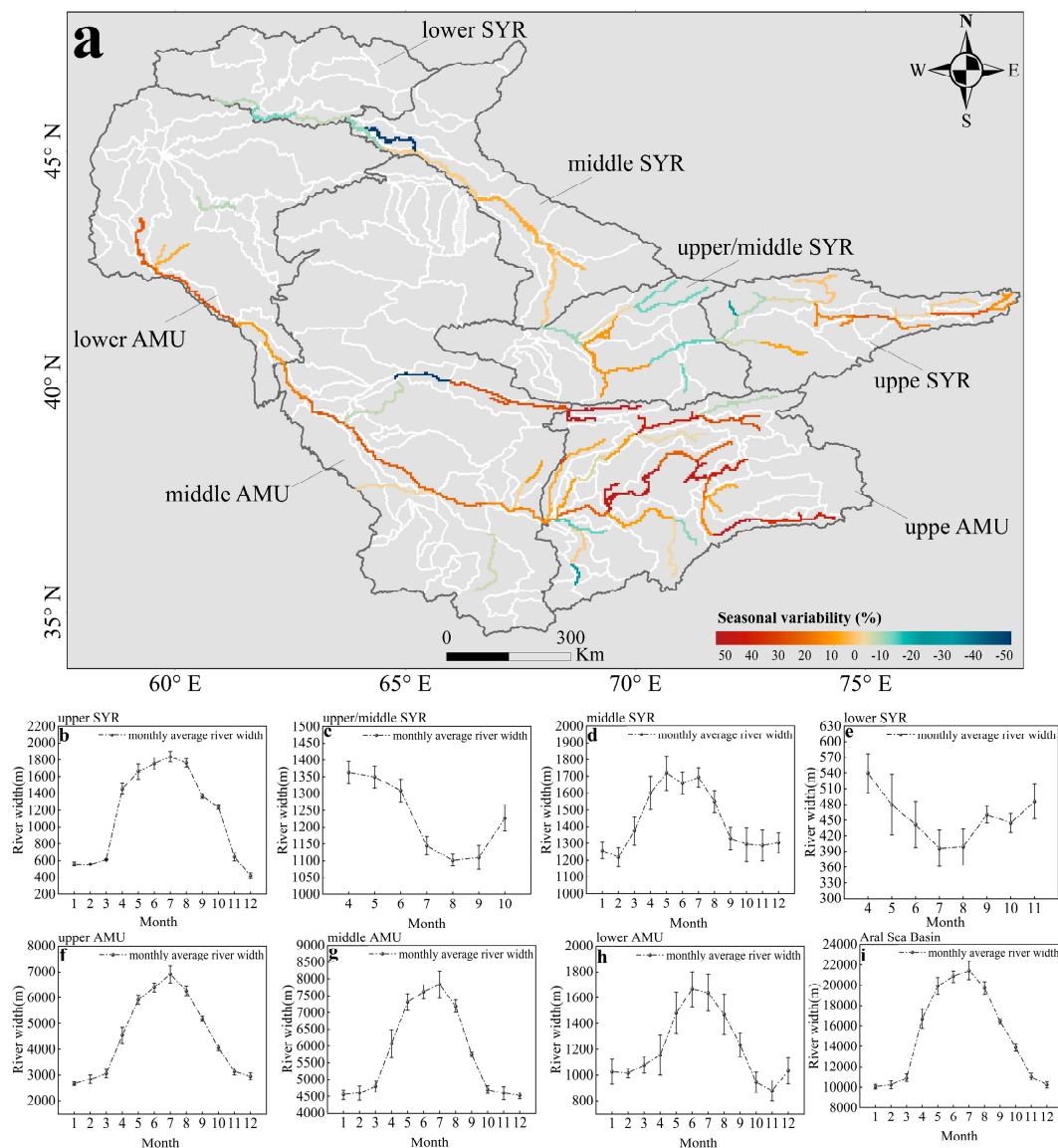


Figure 5. (a) Spatial distribution of seasonal variations and annual dynamics in river width across the seven subregions: (b) upper SYR; (c) upper/middle SYR; (d) middle SYR; (e) lower SYR; (f) upper AMU; (g) middle AMU; (h) lower AMU; (i) the ASB from 2017 to 2022. The average river widths of the upper/middle SYR and lower SYR in the winter were excluded due to the lack of valid observations.

On the other hand, the broader channels observed in the winter can be attributed to ice jams. The middle streams of the Syr Darya experience ice jams due to the relatively gentle stream gradient. In these intermediate parts, which are still frozen, ice is transported from the upper stream, accumulating shattered pieces of ice. In contrast to the tributaries, the mainstem of the Amu Darya showed comparatively less variability.

Figure 5b–h show the seasonal variation curves of the average river width in the seven major subregions. According to the results, the average river width exhibits distinct seasonal patterns: the average river widths in the Amu Darya and Syr Darya upper and middle streams peak in summer. The distinct endorheic nature of the basin is responsible for this observed feature. During the warm season, high temperatures boost the melting of glaciers and snow and increase runoff. However, precipitation peaks occur in the spring and early summer in these regions. As a result, this pattern indicates that the temperature exerted more significant effects on the runoff than precipitation in these areas.

In contrast, the average river width in the upper/middle Syr Darya basin is higher in the spring than in the summer. The average river width in the lower Amu Darya and Syr

Darya reaches its valley value during the warm months. In this region, the winter months bring more precipitation than the summer months. Glacier meltwater contributes relatively little to the downstream river runoff in this region. In addition, river water resources in this region may be affected by human activities. Our analysis provides a clearer understanding of the seasonal variations in the annual river width within the basin. These findings emphasized factors contributing to river width fluctuations, such as temperature and precipitation, and depicted seasonal variations in river width in various regions.

4.1.3. Interannual Variations in River Width

In this study, we conducted an annual time-series analysis based on the annual mean river width computed at the interannual scale to shed light on the temporal dynamics of the river width. Additionally, we plotted the time series from 2017 to 2022 to visualize the interannual variations in the seven major drainage regions.

As shown in Figure 6a, our study results indicate an overall decreasing trend in the river width at the basin scale from 2017 to 2022 in the ASB. The variation trend in the river width shows a high heterogeneity in different types of areas. A decrease in the river width in plain areas is more pronounced, while the river width in high-altitude areas has increased slightly. At the basic scale of river segments, the upstream segments of the basin show an increase in the river width. River segments in the middle and lower reaches have experienced a narrowing in the past several years. Notably, we observed a significant decline near the mouth of the Aral Sea Lake, which corresponds to the river downstream of the Amu Darya. This result highlighted the connection between the Aral Sea crisis and the declining supply of river water resources.

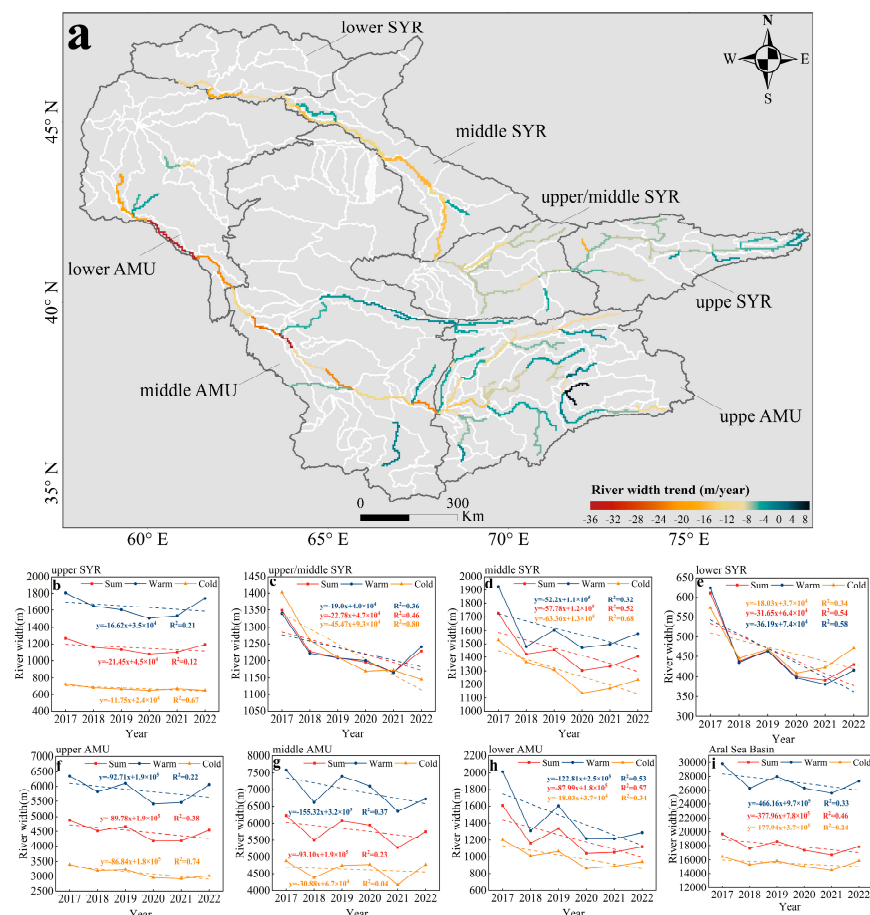


Figure 6. (a) Spatial distribution of river width trends and interannual analysis for (b) upper SYR; (c) upper/middle SYR; (d) middle SYR; (e) lower SYR; (f) upper AMU; (g) middle AMU; (h) lower AMU; (i) the ASB from 2017 to 2022.

The time series of the interannual variation in river widths demonstrates the trends in the different subregions. The mean river width in the whole basin decreased by 1874 m from 19,693 m in 2017 to 17,818 m in 2022, equivalent to a width drop of 378 m/year. Similarly, during the warm and cold seasons, the average river width decreased by 466 m/year and 177 m/year, respectively. The rate of decrease in the river channel width in the warm season is about three times that in the cold season. According to the interannual variation for each sub-basin (Figure 6), the river width variation differs in different subregions from 2017 to 2022 (Figure 6b–h). In particular, compared to the status in 2017, the river widths of all sub-basins fell in 2018, with the amplitude of the decrease being the greatest. In 2019, the river widths in the upper/middle Syr Darya and upper Syr Darya basins decreased while the rest of the sub-basins increased. The river widths in all sub-basins decreased in 2020. In 2021, the river widths fell in the middle Amu Darya and upper/middle Syr Darya while gradually increasing in the remaining regions. In 2022, there was a rising trend in the river width in all sub-basins, but the magnitude of the increase varied.

Our results show that the river width gradually decreased in the basin from 2017 to 2022. The mean river width, on the whole, is in the trend of fluctuation and decline. The most significant decrease in the mean river width occurred in 2018. The mean width decreased by 11.71%, 6.63%, and 10.70% in the warm season, cold season, and whole year, respectively. Although the mean river width tended to increase in 2019 and 2022, the increase was much smaller than the decrease, resulting in narrower rivers throughout the basin overall.

4.2. Comparison with GRWL

To ensure an accurate evaluation of the river extraction results for the ASB, we refrained from directly comparing the absolute river widths between the GRWL and differences in the river extraction results arising from the utilization of distinct sources of images in Sentinel-2 image processing. Alternatively, we evaluate the quality of the river surface extraction results using two criteria: (1) a qualitative evaluation of river completeness and localization accuracy and (2) a quantitative evaluation of the river width. This approach allowed for a comprehensive evaluation of the accuracy. Therefore, we used various validation indicators to evaluate the reliability of the river extraction results obtained from the Sentinel-2 images.

Figure 7 depicts the spatial distribution of the GRWL products and the results of the extracted river in the ASB. Our evaluation reveals that compared to the GRWL dataset, the extracted river networks from the Sentinel-2 images provide more detailed information, including small tributaries in the upper streams. This improved representation is primarily due to using the Sentinel-2 imagery with a higher spatial resolution and applying dynamic thresholds with the Otsu mapping method. Statistics of the river networks between our results and the GRWL dataset (Figure 8) reveal that the average length of connected river reaches from the Sentinel-2 images was approximately 1.9 times longer than that of the GRWL dataset. However, it is crucial to note that the open-water fraction (OWF) extracted from the Sentinel-2 images is only 45% of that in the GRWL dataset. The main reasons for this phenomenon may predominantly include large rivers that influence the open-water fraction, while we detected more small rivers using Sentinel-2 imagery. Consequently, the contribution of narrow rivers to the OWF is relatively limited.

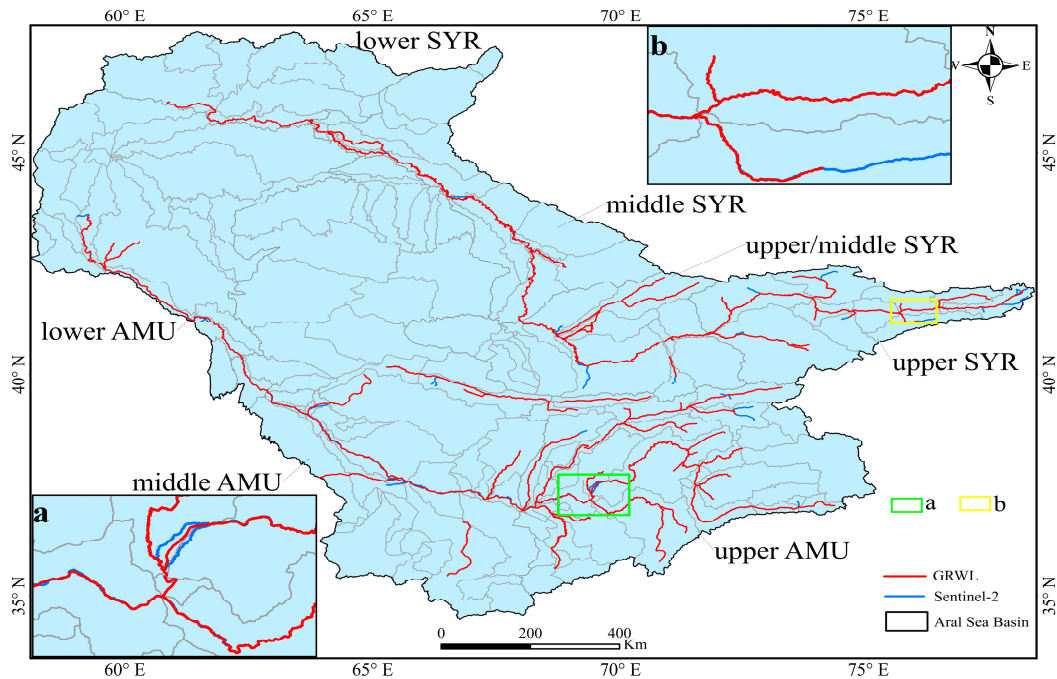


Figure 7. Comparison of the river extraction results from Sentinel-2 and the GRWL centerline products, with zoomed-in maps of (a) the upper reaches of the Amu Darya (37.12°N, 69.36°E) and (b) the upper reaches of the Syr Darya (41.16°N, 75.47°E).

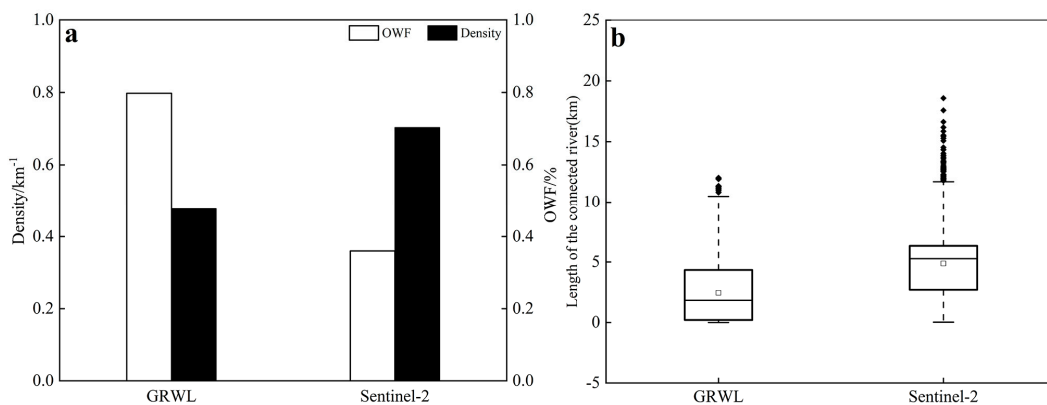


Figure 8. The river extraction results from Sentinel-2 and GRWL dataset are compared with (a) the histogram of river network density and OWF and (b) the connectivity of river network.

5. Discussion

5.1. The Relationship between Seasonal River Width and Climatic Factors

To explore the relationship between the seasonal river width and climatic factors, we calculated the correlation between the monthly river widths and climatic factors in different subregions (Table 2). A significant positive correlation between the temperature and river width was observed in all subregions, excluding the lower Syr Darya and the upper/middle Syr Darya. The positive correlations mean that most rivers in the upper and middle reaches of the Amu Darya and Syr Darya are wider in the warm season. As the snow and glacier melting period in these regions is from June to August [74], the intensified glacier melting in the warm season leads to increased runoff and broader rivers. This is consistent with Aizen (1995) [49], who identified seasonal snowmelt as the primary source of runoff in the headwaters and middle reaches of rivers. Recent studies also revealed that snow cover and glacial meltwater show a higher contribution to river runoff than precipitation in the Tien Shan mountains where the rivers originate [75]. Consequently,

the river width has a higher correlation with the temperature than with precipitation in these regions, which implies that rivers in these regions are predominantly influenced by temperature, as rivers dominated by glacier melt typically exhibit intensified flow peaks from June to September [76]. Meanwhile, evaporation during the warm season is also higher in the Upper SYR, likely driven primarily by temperatures. Therefore, evaporation is positively correlated with the river width.

Table 2. Correlation coefficients between monthly river widths in the ASB and climatic factors.

Region	Temperature	Precipitation	Evaporation
Lower AMU	0.62 **	−0.19	−0.03
Lower SYR	−0.31	0.26 *	0.35 *
Middle AMU	0.85 **	−0.34	−0.02
Middle SYR	0.59 *	−0.17	0.30 *
Upper/middle SYR	−0.35	0.59 **	0.70 **
Upper AMU	0.93 **	−0.28	0.88 **
Upper SYR	0.94 **	0.56 *	0.87 **

Note: ** mean significance at $p < 0.01$ level, * mean significance at $p < 0.05$ level.

The river width is negatively correlated with temperature in the upper Syr Darya and upper/middle Syr Darya basin. In contrast, a positive correlation was found between precipitation and the river width in the regions. Detailed maps show that the river width peaks in the spring (Figure 5) in these basins. As shown in Figure 9, the region receives more precipitation during the cold than the warm season. The major proportion of precipitation occurs in the spring, while the least occurs in the summer in this region [77]. Therefore, the abundant precipitation in the spring dominates the elevated runoff. This result clarifies that rivers in this area are wider in the cold than the warm season and explains that precipitation was the leading supplier of runoff in this sub-basin. In the lower Amu Darya and Syr Darya, the river width attains its minimum value during the summer. As shown in Figure 9, the warm season has higher temperatures and less precipitation in these areas. However, no significant correlations between river widths and climatic factors were observed in either subregion. Notably, the regions in the lower streams of the ASB have a high population density, and irrigated agriculture is mainly concentrated in this area. Therefore, human activities are likely to exert a primary influence on river dynamics.

5.2. The Relationship between Interannual River Width and Climate Variations

Analyzing the temperature change trend in the ASB (Figure 10a), a noticeable increase in the mean annual temperature is observed across the entire basin, with the most significant rises observed in the northwest and southwest regions, excluding the higher-altitude eastern mountains. During the study period, the annual average temperature increased from 9.8 °C to 10.6 °C, with a rise of 0.25 °C per year. This warming rate surpasses the global average of 0.18 °C/10a [78]. A modest increase rate was observed in southern and northeastern regions, contrasted by a substantial rate increase in the southwestern areas. Elevated temperatures accelerate glacier retreat and snowmelt, resulting in heightened river runoff primarily fed by glaciers and snowmelt. Runoff increases with the proportion of glaciers and melting [79].

Simultaneously, the total annual precipitation exhibited a minor increase from 201 mm to 209 mm between 2017 and 2022 (Figure 10d). The ASB demonstrates a significant spatial heterogeneity in precipitation variation. The relatively flat western valleys (Figure 10c) exhibit a noticeable negative trend, experiencing warm and dry weather. In contrast, the eastern high-altitude regions show an increasing trend in precipitation, indicating a relatively humid and cold climate. An analysis of the precipitation trends shows that precipitation in the drought areas of the ASB has decreased in recent years. In contrast, the humid areas have seen an increase in rainfall. This result aligns with the findings reported by Sorg (2012) [80]. Rivers in the upper region expanded over the study period. This phenomenon is not only associated with the accelerated melting of glaciers mentioned

above but may also be related to the significant increase in annual precipitation in the region [54].

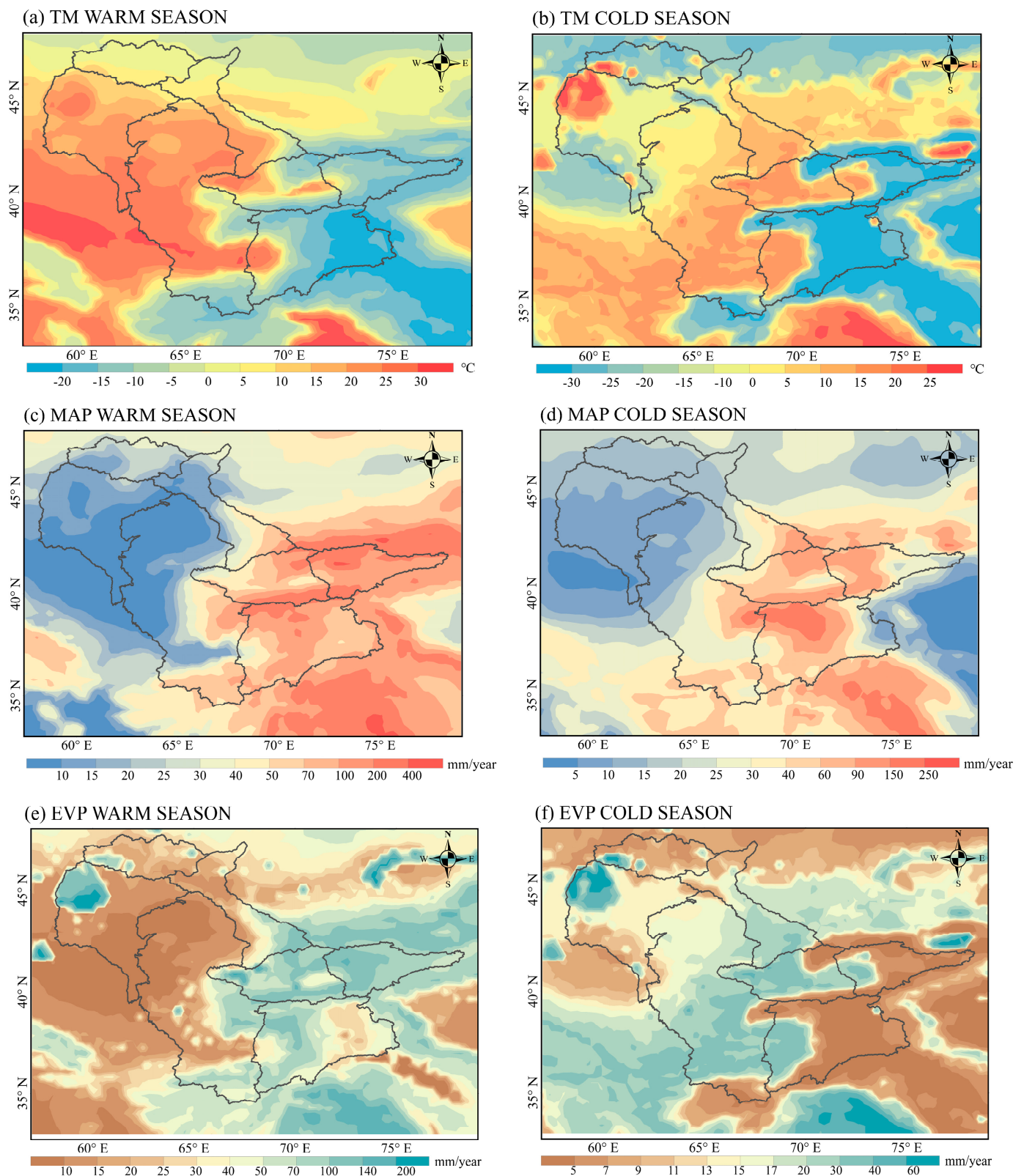


Figure 9. Spatial distributions of different climate variables: mean annual temperature (TM) (a,b), mean annual precipitation (MAP) (c,d), and mean annual evaporation (AET) (e,f) for the warm season and cold season from 2017 to 2022, respectively.

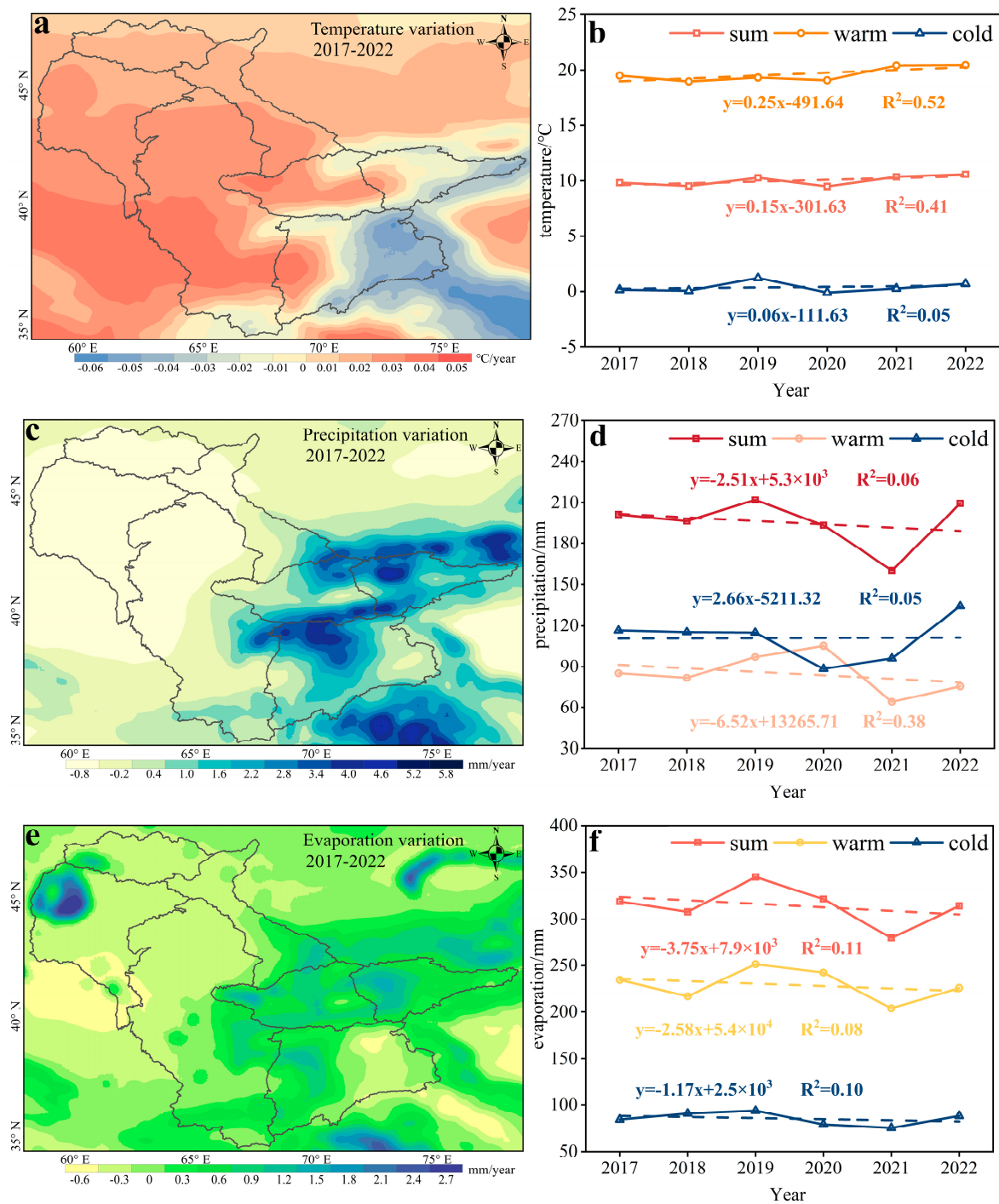


Figure 10. Climate variations in the Aral Sea Basin. Temporal trends in the basin-scale annual mean temperature, total annual precipitation, and total annual evaporation (a,c,e). Spatial trends in the pixel-scale annual mean temperature, total annual precipitation, and total annual evaporation from 2017 to 2022 (b,d,f).

For the spatial variation, evapotranspiration in the basin’s northwestern part increased, especially around the Aral Sea Lake and the southeast mountain region. Simultaneously, the plain area experienced a decline in evaporation in the ASB. The annual total evaporation in the study area ranged between 279 mm and 344 mm during 2017–2022. The annual evapotranspiration exhibited a downward trend in 2018 and 2021 and an upward trend in 2019 and 2022 (Figure 10f). In general, evapotranspiration showed a downward trend, and

the decreasing trend of evapotranspiration in the warm season is about two times that of the cold season.

Despite the relatively short study period, the observed climate changes in this study align with earlier research focusing on long-term climate variations in the ASB. Previous studies have identified a significant annual average temperature increase [81–83]. Most studies agree that there has been a prevailing warming trend in Central Asia, which has accelerated since the 1970s. However, there are discrepancies in the research findings regarding the seasonal changes and the magnitude of warming [84]. Previous research has shown that precipitation variations in the ASB vary between plains and mountains [85,86]. Previous studies indicate that the evaporative demand in the ASB has nearly completely depleted the natural water inflow reaching the Aral Sea [35]. Wider rivers have a larger surface area, which strengthens evaporation because more water can evaporate into the air. Our results show that evapotranspiration near the Aral Sea Lake increased the most, which is consistent with Hu (2019) [87].

5.3. Human Activities on River Dynamics

The river dynamics during the study period may be ascribed to the synergistic impact of climate change and anthropogenic factors. This study investigates how climatic factors impact the river dynamics. Note that anthropogenic factors significantly contribute to river dynamics in the ASB [88]. Human activities greatly influence long-term changes in the Aral Sea [48]. The rivers in the downstream and middle reaches of the basin are considered crucial agricultural production areas in Central Asia and have undergone substantial narrowing. In addition, from 2003 to 2016, the urban areas expanded continuously as the population in the downstream Uzbekistan basin region sharply increased [89]. Expanding farmland and urban areas have increased the demand for water extraction for agricultural irrigation and industrial uses [90]. Issanova (2018) [91] has proposed that the increase in water consumption in Kazakhstan is caused by population growth, leading to an apparent mismatch between the regional demand and supply for water resources. Most rivers in the Amu Darya basin are abstracted for irrigation, particularly in downstream Uzbekistan and Turkmenistan [92]. As the warm season aligns with the growing period for crops that require a substantial water supply [78], the river width reaches its lowest point during the warm season in the lower Amu Darya and Syr Darya.

Simultaneously, cropland has influenced the evapotranspiration patterns in Central Asia, leading to an increase in cropland evapotranspiration. This pattern has, in turn, affected river discharge [93]. Rivers have slightly widened in the upper streams of the basin, which are sparsely populated and belong to non-irrigated areas. Many dams were built in the upstream areas to intercept and store water resources, consequently reducing the downstream flow of the rivers [94]. At the same time, the warming trend in Central Asia has accelerated glacier melting, leading to an increase in river widths in the upstream areas [95]. Human activities have already become a major factor influencing the river dynamics in the ASB. Understanding the link between the anthropogenic factors and river dynamics is important for sustainable water management in this dry region.

6. Summary

This study automatically extracted river water bodies and calculated river widths based on Sentinel-2 images using the Otsu and RivWidth algorithms. We explored the spatiotemporal distribution of river widths and then analyzed the river width variations in each sub-basin in detail from an annual and interannual perspective. We also explored how climatic factors affect river variations. The following summarizes the primary conclusions of this paper:

Rivers are wider in the warm season for the majority of the basin. Almost all rivers in the ASB experienced significant narrowing from 2017 to 2022. In contrast to precipitation, temperature and evaporation have higher correlation values with the river width in most subregions. Higher temperatures caused the glaciers to melt more quickly, which resulted in more significant runoff and wider rivers. Increased temperatures in the Aral Sea

Basin also promoted the increased evaporation of water bodies, especially in the Aral Sea Lake. The results from high-resolution Sentinel-2 imagery provide a more comprehensive spatiotemporal characterization of the river changes than the current dataset. Our results contribute to the improved understanding of river dynamics in the ASB basin, which could assist policymakers in taking effective actions to tackle Central Asia's water resource issues in the future. In addition, the information we provide could be applied to calibrate or validate complex hydrological modeling to assess water resource changes in the region.

With the extension of the high-resolution Sentinel-2 time series, a long-term time-series analysis of river dynamics could be achieved. The automatic extraction method we synthesized can perform detailed and dynamic river monitoring, which can be applied to areas lacking field observations, such as polar and high-altitude mountainous regions, to improve our understanding of climate change effects and hydrological response in the climate-sensitive regions.

Author Contributions: Conceptualization, L.K.; data curation, J.Z. and F.Z.; formal analysis, X.D. and R.W.; funding acquisition, L.K.; investigation, X.D. and R.W.; methodology, J.Z. and F.Z.; project administration, L.K.; resources, F.Z.; software, J.Z.; supervision, L.K.; validation, J.Z.; visualization, L.K.; writing—original draft, J.Z.; writing—review and editing, L.K. All authors have read and agreed to the published version of the manuscript.

Funding: This research was funded by the National Natural Science Foundation of China (Grant No. 42371394) and the Fundamental Research Funds for the Central Universities (B230201031).

Data Availability Statement: The data presented in this study are available on request from the corresponding author. The data are not publicly available due to privacy reasons.

Acknowledgments: We are grateful for the following data providers: ESA for Sentinel-2 images and ERA5-Land product for the meteorological data.

Conflicts of Interest: The authors declare no conflicts of interest.

References

- Oki, T.; Kanae, S. Global Hydrological Cycles and World Water Resources. *Science* **2006**, *313*, 1068–1072. [[CrossRef](#)]
- Feng, D.; Gleason, C.J.; Yang, X.; Pavelsky, T.M. Comparing Discharge Estimates Made via the BAM Algorithm in High-Order Arctic Rivers Derived Solely from Optical CubeSat, Landsat, and Sentinel-2 Data. *Water Resour. Res.* **2019**, *55*, 7753–7771. [[CrossRef](#)]
- Lake, P.S. Ecological effects of perturbation by drought in flowing waters: Effects of drought in streams. *Freshw. Biol.* **2003**, *48*, 1161–1172. [[CrossRef](#)]
- Song, G.-F. Evaluation on water resources and water ecological security with 2-tuple linguistic information. *Int. J. Knowl. Based Intell. Eng. Syst.* **2019**, *23*, 1–8. [[CrossRef](#)]
- Sun, S.; Bao, C.; Fang, C. Freshwater use in China: Relations to economic development and natural water resources availability. *Int. J. Water Resour. Dev.* **2020**, *36*, 738–756. [[CrossRef](#)]
- Bastviken, D.; Tranvik, L.J.; Downing, J.A.; Crill, P.M.; Enrich-Prast, A. Freshwater Methane Emissions Offset the Continental Carbon Sink. *Science* **2011**, *331*, 50. [[CrossRef](#)] [[PubMed](#)]
- Durand, M.; Gleason, C.J.; Garambois, P.A.; Bjerklie, D.; Smith, L.C.; Roux, H.; Rodriguez, E.; Bates, P.D.; Pavelsky, T.M.; Monnier, J.; et al. An intercomparison of remote sensing river discharge estimation algorithms from measurements of river height, width, and slope. *Water Resour. Res.* **2016**, *52*, 4527–4549. [[CrossRef](#)]
- Neal, J.; Schumann, G.; Bates, P. A subgrid channel model for simulating river hydraulics and floodplain inundation over large and data sparse areas: Floodplain inundation over large areas. *Water Resour. Res.* **2012**, *48*. [[CrossRef](#)]
- Gleason, C.J.; Smith, L.C. Toward global mapping of river discharge using satellite images and at-many-stations hydraulic geometry. *Proc. Natl. Acad. Sci. USA* **2014**, *111*, 4788–4791. [[CrossRef](#)] [[PubMed](#)]
- Giustarini, L.; Hostache, R.; Matgen, P.; Schumann, G.J.; Bates, P.D.; Mason, D.C. A Change Detection approach to Flood Mapping in Urban Areas Using TerraSAR-X. *IEEE Trans. Geosci. Remote Sens.* **2013**, *51*, 2417–2430. [[CrossRef](#)]
- Allen, G.H.; Pavelsky, T.M. Global extent of rivers and streams. *Science* **2018**, *361*, 585–588. [[CrossRef](#)]
- Nsubuga, F.W.N.; Botai, J.O.; Olwoch, J.M.; Rautenbach, C.; Kalumba, A.M.; Tsela, P.; Adeola, A.M.; Sentongo, A.A.; Mearns, K.F. Detecting changes in surface water area of Lake Kyoga sub-basin using remotely sensed imagery in a changing climate. *Theor. Appl. Clim.* **2017**, *127*, 327–337. [[CrossRef](#)]
- Pekel, J.-F.; Cottam, A.; Gorelick, N.; Belward, A.S. High-resolution mapping of global surface water and its long-term changes. *Nature* **2016**, *540*, 418–422. [[CrossRef](#)] [[PubMed](#)]

14. Ijaz, M.W.; Siyal, A.A.; Mahar, R.B.; Ahmed, W.; Anjum, M.N. Detection of Hydromorphologic Characteristics of Indus River Estuary, Pakistan, Using Satellite and Field Data. *Arab. J. Sci. Eng.* **2017**, *42*, 2539–2558. [[CrossRef](#)]
15. Wang, C.; Pavlowsky, R.T.; Huang, Q.; Chang, C. Channel bar feature extraction for a mining-contaminated river using high-spatial multispectral remote-sensing imagery. *GISci. Remote Sens.* **2016**, *53*, 283–302. [[CrossRef](#)]
16. Singh, A.; Seitz, F.; Schwatke, C. Inter-annual water storage changes in the Aral Sea from multi-mission satellite altimetry, optical remote sensing, and GRACE satellite gravimetry. *Remote Sens. Environ.* **2012**, *123*, 187–195. [[CrossRef](#)]
17. Psomiadis, E.; Soulis, K.X.; Zoka, M.; Dercas, N. Synergistic Approach of Remote Sensing and GIS Techniques for Flash-Flood Monitoring and Damage Assessment in Thessaly Plain Area, Greece. *Water* **2019**, *11*, 448. [[CrossRef](#)]
18. Huang, C.; Chen, Y.; Zhang, S.; Wu, J. Detecting, Extracting, and Monitoring Surface Water from Space Using Optical Sensors: A Review. *Rev. Geophys.* **2018**, *56*, 333–360. [[CrossRef](#)]
19. Jensen, C.K.; McGuire, K.J.; McLaughlin, D.L.; Scott, D.T. Quantifying spatiotemporal variation in headwater stream length using flow intermittency sensors. *Environ. Monit. Assess.* **2019**, *191*, 226. [[CrossRef](#)]
20. Chen, Q.; Zhang, Y.; Ekroos, A.; Hallikainen, M. The role of remote sensing technology in the EU water framework directive (WFD). *Environ. Sci. Policy* **2004**, *7*, 267–276. [[CrossRef](#)]
21. Avisse, N.; Tilmant, A.; Müller, M.F.; Zhang, H. Monitoring small reservoirs' storage with satellite remote sensing in inaccessible areas. *Hydrol. Earth Syst. Sci.* **2017**, *21*, 6445–6459. [[CrossRef](#)]
22. Donchyts, G.; Schellekens, J.; Winsemius, H.; Eisemann, E.; Van De Giesen, N. A 30 m Resolution Surface Water Mask Including Estimation of Positional and Thematic Differences Using Landsat 8, SRTM and OpenStreetMap: A Case Study in the Murray-Darling Basin, Australia. *Remote Sens.* **2016**, *8*, 386. [[CrossRef](#)]
23. Tortini, R.; Noujdina, N.; Yeo, S.; Ricko, M.; Birkett, C.M.; Khandelwal, A.; Kumar, V.; Marlier, M.E.; Lettenmaier, D.P. Satellite-based remote sensing data set of global surface water storage change from 1992 to 2018. *Earth Syst. Sci. Data* **2020**, *12*, 1141–1151. [[CrossRef](#)]
24. Li, W.; Gong, P. Continuous monitoring of coastline dynamics in western Florida with a 30-year time series of Landsat imagery. *Remote Sens. Environ.* **2016**, *179*, 196–209. [[CrossRef](#)]
25. Tulbure, M.G.; Broich, M.; Stehman, S.V.; Kommareddy, A. Surface water extent dynamics from three decades of seasonally continuous Landsat time series at subcontinental scale in a semi-arid region. *Remote Sens. Environ.* **2016**, *178*, 142–157. [[CrossRef](#)]
26. Wulder, M.A.; White, J.C.; Loveland, T.R.; Woodcock, C.E.; Belward, A.S.; Cohen, W.B.; Fosnight, E.A.; Shaw, J.; Masek, J.G.; Roy, D.P. The global Landsat archive: Status, consolidation, and direction. *Remote Sens. Environ.* **2016**, *185*, 271–283. [[CrossRef](#)]
27. Li, Y.; Niu, Z.; Xu, Z.; Yan, X. Construction of High Spatial-Temporal Water Body Dataset in China Based on Sentinel-1 Archives and GEE. *Remote Sens.* **2020**, *12*, 2413. [[CrossRef](#)]
28. Yamazaki, D.; O'Loughlin, F.; Trigg, M.A.; Miller, Z.F.; Pavelsky, T.M.; Bates, P.D. Development of the Global Width Database for Large Rivers. *Water Resour. Res.* **2014**, *50*, 3467–3480. [[CrossRef](#)]
29. Allen, G.H.; Pavelsky, T.M. Patterns of river width and surface area revealed by the satellite-derived North American River Width data set. *Geophys. Res. Lett.* **2015**, *42*, 395–402. [[CrossRef](#)]
30. Yang, J.; Huang, X.; Tang, Q. Satellite-derived river width and its spatiotemporal patterns in China during 1990–2015. *Remote Sens. Environ.* **2020**, *247*, 111918. [[CrossRef](#)]
31. Drusch, M.; Del Bello, U.; Carlier, S.; Colin, O.; Fernandez, V.; Gascon, F.; Hoersch, B.; Isola, C.; Laberinti, P.; Martimort, P.; et al. Sentinel-2: ESA's Optical High-Resolution Mission for GMES Operational Services. *Remote Sens. Environ.* **2012**, *120*, 25–36. [[CrossRef](#)]
32. Du, Y.; Zhang, Y.; Ling, F.; Wang, Q.; Li, W.; Li, X. Water Bodies' Mapping from Sentinel-2 Imagery with Modified Normalized Difference Water Index at 10-m Spatial Resolution Produced by Sharpening the SWIR Band. *Remote Sens.* **2016**, *8*, 354. [[CrossRef](#)]

33. Yesou, H.; Pottier, E.; Mercier, G.; Grizonnet, M.; Haouet, S.; Giros, A.; Faivre, R.; Huber, C.; Michel, J. Synergy of Sentinel-1 and Sentinel-2 imagery for wetland monitoring information extraction from continuous flow of sentinel images applied to water bodies and vegetation mapping and monitoring. In Proceedings of the 2016 IEEE International Geoscience and Remote Sensing Symposium (IGARSS), Beijing, China, 10–15 July 2016; pp. 162–165. [\[CrossRef\]](#)
34. Ogilvie, A.; Belaud, G.; Massuel, S.; Mulligan, M.; Le Goulven, P.; Calvez, R. Surface water monitoring in small water bodies: Potential and limits of multi-sensor Landsat time series. *Hydrol. Earth Syst. Sci.* **2018**, *22*, 4349–4380. [\[CrossRef\]](#)
35. Huang, S.; Chen, X.; Chang, C.; Liu, T.; Huang, Y.; Zan, C.; Ma, X.; De Maeyer, P.; Van de Voorde, T. Impacts of climate change and evapotranspiration on shrinkage of Aral Sea. *Sci. Total Environ.* **2022**, *845*, 157203. [\[CrossRef\]](#) [\[PubMed\]](#)
36. Schiermeier, Q. Ecologists plot to turn the tide for shrinking lake. *Nature* **2001**, *412*, 756. [\[CrossRef\]](#) [\[PubMed\]](#)
37. Chen, X.; Zuo, H.; Wang, W.; Duan, J.; Chang, M.; Wang, J. Surface water and aerosol spatiotemporal dynamics and influence mechanisms over drylands. *Geosci. Front.* **2023**, *14*, 101524. [\[CrossRef\]](#)
38. Abdullaev, I. Water Management Policies of Central Asian Countries: Integration or Disintegration? In Proceedings of the USDS Organized Conference Celebrating 10 Years of Contemporary Issues Fellowships Conference on Water Issues in Central Asia, Tashkent, Uzbekistan, 25 September 2004.
39. Klein, I.; Dietz, A.J.; Gessner, U.; Galayeva, A.; Myrzakhmetov, A.; Kuenzer, C. Evaluation of seasonal water body extents in Central Asia over the past 27 years derived from medium-resolution remote sensing data. *Int. J. Appl. Earth Obs. Geoinf.* **2014**, *26*, 335–349. [\[CrossRef\]](#)
40. Che, X.; Feng, M.; Sun, Q.; Sexton, J.O.; Channan, S.; Liu, J. The Decrease in Lake Numbers and Areas in Central Asia Investigated Using a Landsat-Derived Water Dataset. *Remote Sens.* **2021**, *13*, 1032. [\[CrossRef\]](#)
41. Azzam, A.; Zhang, W.; Xu, C.; Khan, Z. Calibration and evaluation of Hargreaves-Samani equation for estimating reference evapotranspiration: A case study in the Amu Darya River Basin, Central Asia. *J. Hydrol. Reg. Stud.* **2023**, *45*, 101298. [\[CrossRef\]](#)
42. Sorrel, P.; Popescu, S.-M.; Klotz, S.; Suc, J.-P.; Oberhänsli, H. Climate variability in the Aral Sea basin (Central Asia) during the late Holocene based on vegetation changes. *Quat. Res.* **2007**, *67*, 357–370. [\[CrossRef\]](#)
43. Bocchiola, D.; Pelosi, M.G.; Soncini, A. Effects of hydrological changes on cooperation in transnational catchments: The case of the Syr Darya. *Water Int.* **2017**, *42*, 852–873. [\[CrossRef\]](#)
44. Jarsjö, J.; Asokan, S.M.; Prieto, C.; Bring, A.; Destouni, G. Hydrological responses to climate change conditioned by historic alterations of land-use and water-use. *Hydrol. Earth Syst. Sci.* **2012**, *16*, 1335–1347. [\[CrossRef\]](#)
45. Nuimura, T.; Sakai, A.; Taniguchi, K.; Nagai, H.; Lamsal, D.; Tsutaki, S.; Kozawa, A.; Hoshina, Y.; Takenaka, S.; Omiya, S.; et al. The GAMDAM glacier inventory: A quality-controlled inventory of Asian glaciers. *Cryosphere* **2015**, *9*, 849–864. [\[CrossRef\]](#)
46. Nezlin, N.P.; Kostianoy, A.G.; Lebedev, S.A. Interannual variations of the discharge of Amu Darya and Syr Darya estimated from global atmospheric precipitation. *J. Mar. Syst.* **2004**, *47*, 67–75. [\[CrossRef\]](#)
47. Zhang, M.; Chen, Y.; Shen, Y.; Li, Y. Changes of precipitation extremes in arid Central Asia. *Quat. Int.* **2017**, *436*, 16–27. [\[CrossRef\]](#)
48. Yang, X.; Wang, N.; Chen, A.; He, J.; Hua, T.; Qie, Y. Changes in area and water volume of the Aral Sea in the arid Central Asia over the period of 1960–2018 and their causes. *CATENA* **2020**, *191*, 104566. [\[CrossRef\]](#)
49. Aizen, V.B.; Aizen, E.M.; Melack, J.M. Climate, Snow Cover, Glaciers, and Runoff in the Tien Shan, Central Asia. *JAWRA J. Am. Water Resour. Assoc.* **1995**, *31*, 1113–1129. [\[CrossRef\]](#)
50. Schiemann, R.; Lüthi, D.; Vidale, P.L.; Schär, C. The precipitation climate of Central Asia—Intercomparison of observational and numerical data sources in a remote semiarid region. *Int. J. Clim.* **2008**, *28*, 295–314. [\[CrossRef\]](#)
51. Chen, X.; Wang, S.; Hu, Z.; Zhou, Q.; Hu, Q. Spatiotemporal characteristics of seasonal precipitation and their relationships with ENSO in Central Asia during 1901–2013. *J. Geogr. Sci.* **2018**, *28*, 1341–1368. [\[CrossRef\]](#)
52. Hu, Z.; Zhou, Q.; Chen, X.; Qian, C.; Wang, S.; Li, J. Variations and changes of annual precipitation in Central Asia over the last century. *Int. J. Clim.* **2017**, *37*, 157–170. [\[CrossRef\]](#)
53. Berdimbetov, T.T.; Ma, Z.-G.; Liang, C.; Ilyas, S. Impact of Climate Factors and Human Activities on Water Resources in the Aral Sea Basin. *Hydrology* **2020**, *7*, 30. [\[CrossRef\]](#)
54. Wang, X.; Chen, Y.; Li, Z.; Fang, G.; Wang, F.; Liu, H. The impact of climate change and human activities on the Aral Sea Basin over the past 50 years. *Atmos. Res.* **2020**, *245*, 105125. [\[CrossRef\]](#)
55. Yang, X.; Zhao, S.; Qin, X.; Zhao, N.; Liang, L. Mapping of Urban Surface Water Bodies from Sentinel-2 MSI Imagery at 10 m Resolution via NDWI-Based Image Sharpening. *Remote Sens.* **2017**, *9*, 596. [\[CrossRef\]](#)
56. Verdin, K.; Verdin, J. A topological system for delineation and codification of the Earth's river basins. *J. Hydrol.* **1999**, *218*, 1–12. [\[CrossRef\]](#)
57. Nagaveni, C.; Kumar, K.P.; Ravibabu, M.V. Evaluation of TanDEMx and SRTM DEM on watershed simulated runoff estimation. *J. Earth Syst. Sci.* **2019**, *128*, 2. [\[CrossRef\]](#)
58. Nobre, A.D.; Cuartas, L.A.; Hodnett, M.; Rennó, C.D.; Rodrigues, G.; Silveira, A.; Waterloo, M.; Saleska, S. Height Above the Nearest Drainage—A hydrologically relevant new terrain model. *J. Hydrol.* **2011**, *404*, 13–29. [\[CrossRef\]](#)
59. Muñoz-Sabater, J.; Dutra, E.; Agustí-Panareda, A.; Albergel, C.; Arduini, G.; Balsamo, G.; Boussetta, S.; Choulga, M.; Harrigan, S.; Hersbach, H.; et al. ERA5-Land: A state-of-the-art global reanalysis dataset for land applications. *Earth Syst. Sci. Data* **2021**, *13*, 4349–4383. [\[CrossRef\]](#)
60. Pavelsky, T.M.; Smith, L.C. RivWidth: A Software Tool for the Calculation of River Widths from Remotely Sensed Imagery. *IEEE Geosci. Remote Sens. Lett.* **2008**, *5*, 70–73. [\[CrossRef\]](#)

61. McFeeters, S.K. The use of the Normalized Difference Water Index (NDWI) in the delineation of open water features. *Int. J. Remote Sens.* **1996**, *17*, 1425–1432. [[CrossRef](#)]
62. Xu, H. Modification of normalised difference water index (NDWI) to enhance open water features in remotely sensed imagery. *Int. J. Remote Sens.* **2006**, *27*, 3025–3033. [[CrossRef](#)]
63. Ji, L.; Zhang, L.; Wylie, B. Analysis of Dynamic Thresholds for the Normalized Difference Water Index. *Photogramm. Eng. Remote Sens.* **2009**, *75*, 1307–1317. [[CrossRef](#)]
64. Singh, K.V.; Setia, R.; Sahoo, S.; Prasad, A.; Pateriya, B. Evaluation of NDWI and MNDWI for assessment of waterlogging by integrating digital elevation model and groundwater level. *Geocarto Int.* **2015**, *30*, 650–661. [[CrossRef](#)]
65. Lawal, A.; Kerner, H.; Becker-Reshef, I.; Meyer, S. Mapping the Location and Extent of 2019 Prevent Planting Acres in South Dakota Using Remote Sensing Techniques. *Remote Sens.* **2021**, *13*, 2430. [[CrossRef](#)]
66. Sun, F.; Sun, W.; Chen, J.; Gong, P. Comparison and improvement of methods for identifying waterbodies in remotely sensed imagery. *Int. J. Remote Sens.* **2012**, *33*, 6854–6875. [[CrossRef](#)]
67. Chini, M.; Hostache, R.; Giustarini, L.; Matgen, P. A Hierarchical Split-Based Approach for Parametric Thresholding of SAR Images: Flood Inundation as a Test Case. *IEEE Trans. Geosci. Remote Sens.* **2017**, *55*, 6975–6988. [[CrossRef](#)]
68. Xu-Kai, Z.; Xia, Z.; Qiong-Qiong, L.; Baig, M.H.A. Automated detection of coastline using Landsat TM based on water index and edge detection methods. In Proceedings of the 2012 Second International Workshop on Earth Observation and Remote Sensing Applications (EORSA), Shanghai, China, 8–11 June 2012; pp. 153–156.
69. Sheng, Y.; Song, C.; Wang, J.; Lyons, E.A.; Knox, B.R.; Cox, J.S.; Gao, F. Representative lake water extent mapping at continental scales using multi-temporal Landsat-8 imagery. *Remote Sens. Environ.* **2016**, *185*, 129–141. [[CrossRef](#)]
70. Li, N.; Lv, X.; Xu, S.; Li, B.; Gu, Y. An Improved Water Surface Images Segmentation Algorithm Based on the Otsu Method. *J. Circuits Syst. Comput.* **2020**, *29*, 2050251. [[CrossRef](#)]
71. Otsu, N. A threshold selection method from gray-level histograms. *IEEE Trans. Syst. Man Cybern.* **1979**, *9*, 62–66. [[CrossRef](#)]
72. Puth, M.-T.; Neuhäuser, M.; Ruxton, G.D. Effective use of Pearson’s product–moment correlation coefficient. *Anim. Behav.* **2014**, *93*, 183–189. [[CrossRef](#)]
73. Yuan, Y.; Zeng, G.; Liang, J.; Huang, L.; Hua, S.; Li, F.; Zhu, Y.; Wu, H.; Liu, J.; He, X.; et al. Variation of water level in Dongting Lake over a 50-year period: Implications for the impacts of anthropogenic and climatic factors. *J. Hydrol.* **2015**, *525*, 450–456. [[CrossRef](#)]
74. Shahgedanova, M.; Afzal, M.; Severskiy, I.; Usmanova, Z.; Saidaliyeva, Z.; Kapitsa, V.; Kasatkin, N.; Dolgikh, S. Changes in the mountain river discharge in the northern Tien Shan since the mid-20th Century: Results from the analysis of a homogeneous daily streamflow data set from seven catchments. *J. Hydrol.* **2018**, *564*, 1133–1152. [[CrossRef](#)]
75. Chen, H.; Chen, Y.; Li, W.; Li, Z. Quantifying the contributions of snow/glacier meltwater to river runoff in the Tianshan Mountains, Central Asia. *Glob. Planet. Chang.* **2019**, *174*, 47–57. [[CrossRef](#)]
76. Ward, F.A.; Pulido-Velazquez, M. Water conservation in irrigation can increase water use. *Proc. Natl. Acad. Sci. USA* **2008**, *105*, 18215–18220. [[CrossRef](#)]
77. Kriegel, D.; Mayer, C.; Hagg, W.; Vorogushyn, S.; Duethmann, D.; Gafurov, A.; Farinotti, D. Changes in glacierisation, climate and runoff in the second half of the 20th century in the Naryn basin, Central Asia. *Glob. Planet. Chang.* **2013**, *110*, 51–61. [[CrossRef](#)]
78. Jones, P.D.; Lister, D.H.; Osborn, T.J.; Harpham, C.; Salmon, M.; Morice, C.P. Hemispheric and large-scale land-surface air temperature variations: An extensive revision and an update to 2010. *J. Geophys. Res. Atmos.* **2012**, *117*, 2011JD017139. [[CrossRef](#)]
79. Zhang, Y.; Luo, Y.; Sun, L.; Liu, S.; Chen, X.; Wang, X. Using glacier area ratio to quantify effects of melt water on runoff. *J. Hydrol.* **2016**, *538*, 269–277. [[CrossRef](#)]
80. Sorg, A.; Bolch, T.; Stoffel, M.; Solomina, O.; Beniston, M. Climate change impacts on glaciers and runoff in Tien Shan (Central Asia). *Nat. Clim. Chang.* **2012**, *2*, 725–731. [[CrossRef](#)]
81. Hu, Z.; Zhang, C.; Hu, Q.; Tian, H. Temperature Changes in Central Asia from 1979 to 2011 Based on Multiple Datasets*. *J. Clim.* **2014**, *27*, 1143–1167. [[CrossRef](#)]
82. Chen, F.; Wang, J.; Jin, L.; Zhang, Q.; Li, J.; Chen, J. Rapid warming in mid-latitude central Asia for the past 100 years. *Front. Earth Sci. China* **2009**, *3*, 42–50. [[CrossRef](#)]
83. Chen, Z.; Chen, Y.; Bai, L.; Xu, J. Multiscale evolution of surface air temperature in the arid region of Northwest China and its linkages to ocean oscillations. *Theor. Appl. Clim.* **2017**, *128*, 945–958. [[CrossRef](#)]
84. Unger-Shayesteh, K.; Vorogushyn, S.; Farinotti, D.; Gafurov, A.; Duethmann, D.; Mandychev, A.; Merz, B. What do we know about past changes in the water cycle of Central Asian headwaters? A review. *Glob. Planet. Chang.* **2013**, *110*, 4–25. [[CrossRef](#)]
85. Deng, H.; Chen, Y. Influences of recent climate change and human activities on water storage variations in Central Asia. *J. Hydrol.* **2017**, *544*, 46–57. [[CrossRef](#)]
86. Haag, I.; Jones, P.D.; Samimi, C. Central Asia’s Changing Climate: How Temperature and Precipitation Have Changed across Time, Space, and Altitude. *Climate* **2019**, *7*, 123. [[CrossRef](#)]
87. Hu, Z.; Zhou, Q.; Chen, X.; Chen, D.; Li, J.; Guo, M.; Yin, G.; Duan, Z. Groundwater Depletion Estimated from GRACE: A Challenge of Sustainable Development in an Arid Region of Central Asia. *Remote Sens.* **2019**, *11*, 1908. [[CrossRef](#)]
88. Philip, M. Aral Sea Basin Water Resources and the Changing Aral Water Balance. In *The Aral Sea*; Micklin, P., Aladin, N.V., Plotnikov, I., Eds.; Springer: Berlin/Heidelberg, Germany, 2014; pp. 111–135. [[CrossRef](#)]

89. Zhou, Y.; Zhang, L.; Xiao, J.; Williams, C.A.; Vitkovskaya, I.; Bao, A. Spatiotemporal transition of institutional and socioeconomic impacts on vegetation productivity in Central Asia over last three decades. *Sci. Total Environ.* **2019**, *658*, 922–935. [[CrossRef](#)]
90. Lothar, M.; Suleimenov, M.; Karimov, A.; Qadir, M.; Saparov, A.; Balgabayev, N.; Helming, K.; Lischeid, G. Land and Water Resources of Central Asia, Their Utilisation and Ecological Status. In *Novel Measurement and Assessment Tools for Monitoring and Management of Land and Water Resources in Agricultural Landscapes of Central Asia*; Mueller, L., Saparov, A., Lischeid, G., Eds.; Environmental Science and Engineering; Springer International Publishing: Cham, Switzerland, 2014; pp. 3–59. [[CrossRef](#)]
91. Issanova, G.; Jilili, R.; Abuduwaili, J.; Kaldybayev, A.; Saparov, G.; Yongxiao, G. Water availability and state of water resources within water-economic basins in Kazakhstan. *Paddy Water Environ.* **2018**, *16*, 183–191. [[CrossRef](#)]
92. Schlüter, M.; Khasankhanova, G.; Talskikh, V.; Taryannikova, R.; Agaltseva, N.; Joldasova, I.; Ibragimov, R.; Abdullaev, U. Enhancing resilience to water flow uncertainty by integrating environmental flows into water management in the Amudarya River, Central Asia. *Glob. Planet. Chang.* **2013**, *110*, 114–129. [[CrossRef](#)]
93. Shibuo, Y.; Jarsjö, J.; Destouni, G. Hydrological responses to climate change and irrigation in the Aral Sea drainage basin. *Geophys. Res. Lett.* **2007**, *34*, 2007GL031465. [[CrossRef](#)]
94. Lehner, B.; Liermann, C.R.; Revenga, C.; Vorosmarty, C.; Fekete, B.; Crouzet, P.; Döll, P.; Endejan, M.; Frenken, K.; Magome, J.; et al. High-resolution mapping of the world's reservoirs and dams for sustainable river-flow management. *Front. Ecol. Environ.* **2011**, *9*, 494–502. [[CrossRef](#)]
95. Chen, H.; Liu, H.; Chen, X.; Qiao, Y. Analysis on impacts of hydro-climatic changes and human activities on available water changes in Central Asia. *Sci. Total Environ.* **2020**, *737*, 139779. [[CrossRef](#)]

Disclaimer/Publisher's Note: The statements, opinions and data contained in all publications are solely those of the individual author(s) and contributor(s) and not of MDPI and/or the editor(s). MDPI and/or the editor(s) disclaim responsibility for any injury to people or property resulting from any ideas, methods, instructions or products referred to in the content.